PAPER

WO₃ nanosponge photoanodes with high applied bias photon-to-current efficiency for solar hydrogen and peroxydisulfate production†

Tomohiko Nakajima,*[a] Aya Hagino,[a] Takako Nakamura,[a] Tetsuo Tsuchiya[a] and Kazuhiro Sayama[b]

We prepared WO₃ nanosponge photoanodes by nanoparticle/solution hybrid dispersion–deposition. The WO₃ nanosponge photoanodes showed a large photocurrent (3.04 mA cm^{-2}) in 1.0 M H$_2$SO$_4$ electrolyte under 1 Sun illumination. This high photocurrent arose from the robust inter-nanoparticle connections and preservation of the nanopores in the photoanode, achieved by the addition of tungsten phenoxide and the very fine nanoparticles obtained by wet milling. The absorbed photon-to-current efficiency spectra showed a high maximum of 95.4% at 410 nm. The Faraday efficiency of S$_2$O$_8^{2-}$ and H$_2$ evolution was almost 100%, and the applied bias photon-to-current efficiency for S$_2$O$_8^{2-}$ and H$_2$ was calculated to be 2.45%, which is the highest reported value. Obtaining this kind of high-value-added product efficiently at photoanodes in photoelectrochemical systems is important for the use of sunlight in sustainable industrial chemistry.

Introduction

Solar hydrogen production has great potential as a sustainable green energy source.[1-6] In particular, the use of semiconductor photoelectrodes for solar water splitting has been studied extensively,[7-11] because photoelectrochemical (PEC) systems have the following major advantages for water splitting: (1) easing the energy level restrictions in semiconductor photoelectrodes by using an external bias voltage; and (2) allowing charge separation and straightforward product collection at separate reaction sites for oxidation (anode) and reduction (cathode). There have been numerous reports on water splitting in PEC systems,[12-19] and TiO₂ and WO₃ photoelectrodes have been widely used because of their high chemical stability. Although pure TiO₂ shows high activity under only ultraviolet (UV) light due to its wide band gap at 3.2 eV,[20-22] black TiO₂, to which hydrogen and anions (S, N, and I), or oxygen deficiencies have been introduced, has achieved an enhanced photoresponse, even under sunlight.[23-25] Black TiO₂ photoelectrode systems showed an increase in the solar-to-hydrogen (STH) efficiency of 1.5–2.0%.

Solar hydrogen production from water is an important goal for energy production; however, the current STH efficiency is still not commercially feasible. The STH efficiency should stably exceed 10–20%.[26,27] Thus, we have been searching for other applications of photoelectrodes driven by sunlight. Solar hydrogen production in PEC systems is a cathode reaction, and oxygen gas is obtained at the photoanodes. Oxygen gas has a market value less than several tens of percent that of hydrogen gas, and few studies have focused on the other products besides oxygen at photoanodes. However, Mi et al. reported that some products, such as peroxydisulfate (S$_2$O$_8^{2-}$) and H$_2$O$_2$, can be obtained at WO₃ photoanodes in aqueous electrolytes.[28] Fuku et al. obtained Ce^{4+}, IO$_4^-$, and H$_2$O$_2$ in the WO₃ photoanode system in addition to S$_2$O$_8^{2-}$.[29,30] These reagents have a much higher market value than oxygen. In this work, we focused on the availability of these high-value-added anode products obtained by PEC solar hydrogen production. For example, S$_2$O$_8^{2-}$ is important as an industrial bleaching and oxidising reagent, and it generally has a market price more than one hundred times that of oxygen. Therefore, peroxydisulfate evolution at the photoanode in addition to hydrogen gas evolution at the cathode is a possible application of sunlight. The peroxydisulfate ions were evolved by an anion-derived hole transfer process in accordance with the following equation reported by Mi et al.:[28]

$$2HSO_4^- \rightarrow S_2O_8^{2-} + 2H^+ + 2e^-,$$
$$S_2O_8^{2-}/HSO_4^- = +2.12 \text{ V } vs. \text{ RHE} \quad (1)$$
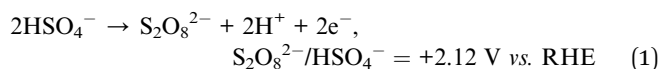
[a]Advanced Coating Technology Research Center, National Institute of Advanced Industrial Science and Technology, Tsukuba Central 5, 1-1-1 Higashi, Tsukuba, Ibaraki 305-8565, Japan. E-mail: t-nakajima@aist.go.jp; Tel: +81-29-861-6368

[b]Research Center for Photovoltaics, National Institute of Advanced Industrial Science and Technology, Tsukuba Central 5, 1-1-1 Higashi, Tsukuba, Ibaraki 305-8565, Japan

This journal is © The Royal Society of Chemistry 2016

J. Mater. Chem. A, 2016, 4, 17809–17818 | 17809

The present highest applied bias photon-to-current efficiency for $S_2O_8^{2-}$ and H_2 ($ABPE_{S_2O_8^{2-}}$) is 2.2% in WO_3 photoanodes.[29] WO_3 photoanodes have a narrower band gap (2.6–2.8 eV) than TiO_2 and are highly stable under acidic conditions. In addition, they have a deep valence band potential at +3.0 eV; thus, WO_3 photoanodes are suitable for obtaining various oxidants under sunlight. However, the reported value of the photocurrent in the WO_3 photoanodes (single junction) for water splitting[15,31,32] generally remains 1.0–2.5 mA cm^{-2} under simulated sunlight (AM1.5G), which is far below the theoretical limit[33] of the photocurrent of other semiconductor photoanodes. Therefore, the fabrication process for WO_3 photoanodes must be improved to realize the potential of the material. We refocused on effective nanostructures for maximizing PEC properties in the WO_3. The excited electron/hole transporting property is one of the most important key factors for enhancing PEC reactions. While there are many reports on a fabrication process for interparticle necking to enhance transporting properties in TiO_2 photoelectrodes,[34,35] it has been rarely studied in the WO_3. In this study, we have developed a new WO_3 nanoparticle/solution (NPS) hybrid dispersion–deposition process to make rigid inter-particle connections in the WO_3 nanostructure. The obtained WO_3 nanosponge photoanodes prepared by using this fabrication process showed very high photocurrent and a maximum $ABPE_{S_2O_8^{2-}}$ of 2.45%.

Experimental procedure

Preparation and characterisation of WO₃ nanosponge layers

A WO_3 nanoparticle dispersion was prepared by wet-ball milling of WO_3 nanocrystal powders (EM Japan) in isopropanol (IPA) with a tilted rotation planetary ball mill (Planet M, Nagao System) using zirconia balls at 650 rpm with or without a toluene solution of tungsten phenoxide (Gelest) as a source of W ions in the dispersion ink. The dispersion containing WO_3 nanocrystals and W ion solution is called WO_3 NPS hybrid dispersion ink. Polyethylene glycol (PEG; molecular weight: 300, Wako Pure Chemical) was added to the WO_3 dispersion ink in a 1 : 1 volume ratio. The WO_3 dispersion ink with PEG was spin-coated at 2000 rpm for 10 s onto F-doped SnO_2 (FTO) glass substrates. The films were preheated at 500 °C for 5 min. The coating and preheating were repeated several times to increase the film thickness, and then the preheated films were fired at 550 °C for 30 min in air. The preparation conditions and film thickness of representative photoanodes are shown in Table 1. The phase purity and crystallinity of the WO_3 thin films on the FTO substrates were determined by X-ray diffraction (XRD;

SmartLab, Rigaku). The distribution of particle size (d) for the WO_3 dispersion was checked with a particle size analyser (ELSZ-1000, Otsuka Electronics). The surface morphology and cross-sectional structure were determined by field emission scanning electron microscopy (FESEM; SU9000, Hitachi). The optical absorbance spectra and light harvesting efficiency (LHE) of the WO_3 films were evaluated by using a UV-visible spectrometer (UV-3150, Shimadzu) equipped with an integrating sphere (MPC-3100, Shimadzu). X-ray photoemission spectroscopy (XPS) was carried out with an Al Kα source.

PEC performance evaluation

Linear sweep voltammetry for solar water splitting photocurrent measurements was performed under 100 mW cm^{-2} AM 1.5G simulated sunlight (1 Sun) from a 150 W Xe lamp (XES-40S2-CE, San-Ei Electric), in 1.0 M H_2SO_4 (pH = 0.0) at 0.4–2.0 V vs. a reversible hydrogen electrode (V_{RHE}) in a three-electrode electrochemical cell equipped with a quartz glass window. The 1 Sun simulated sunlight was calibrated by using a spectroradiometer (Fig. S1;† SOMA Optics). An Ag/AgCl reference electrode in saturated KCl solution and a Pt wire counter electrode were used, and the scan rate was 5 mV s^{-1}. The measured potential vs. Ag/AgCl ($V_{Ag/AgCl}$) in the three-electrode system was converted to V_{RHE} according to $V_{RHE} = V_{Ag/AgCl} + 0.059pH + V^0_{Ag/AgCl}$, where $V^0_{Ag/AgCl} = 0.1976$ at 25 °C. Mott–Schottky plots were obtained by using a potentiostat (Autolab PGSTAT204, Metrohm) equipped with an impedance analyser (Autolab FRA32M, Metrohm) in 1 M H_2SO_4. The excitation voltage and frequency were 10 mV and 1 kHz, respectively. Intensity modulated photocurrent spectroscopy (IMPS) was performed with a potentiostat (PGSTAT204, Metrohm), an impedance analyser (FRA32M, Metrohm), and a light-emitting diode (LED) driver kit (Metrohm) that drove a 365 nm power UV LED (NCSU033B, Hamamatsu Photonics). The LED intensity was modulated by 10% in the range of 100 kHz–0.1 Hz. Incident photon-to-current conversion efficiency (IPCE) was evaluated by using the three-electrode setup with the equation IPCE = $1240J/\lambda I$, where λ is the incident light wavelength (nm), and I is the intensity of the light source at each wavelength (mW cm^{-2}). The absorbed photon-to-current efficiency (APCE) was calculated by APCE = IPCE/LHE. The bias voltage was $1.50V_{RHE}$. The monochromatic light was generated by a Xe lamp with a monochromator (SPG-120S-REV, Shimadzu). The $ABPE_{S_2O_8^{2-}}$ of the WO_3 photoanodes was measured by using a two-electrode configuration cell with a Pt wire counter electrode and an ion-exchange membrane (Nafion). $ABPE_{S_2O_8^{2-}}$ values were estimated by $ABPE_{S_2O_8^{2-}} = J(2.12 - E_{CE})\eta(S_2O_8^{2-})/I_{AM1.5}$, where J is the photocurrent density (mA cm^{-2}), E_{CE} is the applied bias voltage

Table 1 Preparation conditions and thickness of representative photoanodes

Sample	Thickness/μm	Dispersion	WO₃ nanoparticle/wt%	W phenoxide/mM	Milling time/min
W1	7.3(4)	D1	10	0.0	15
W2	7.3(2)	D2	23	0.0	360
W3	7.4(5)	D3	23	5.0	360

17810 | *J. Mater. Chem. A*, 2016, **4**, 17809–17818

This journal is © The Royal Society of Chemistry 2016

vs. the counter electrode, $\eta(S_2O_8{}^{2-})$ is the Faraday efficiency of $S_2O_8{}^{2-}$ production, and $I_{AM1.5}$ is the irradiance of AM 1.5 simulated sunlight at 100 mW cm^{-2}. The production of $S_2O_8{}^{2-}$ was evaluated by colorimetry by using UV-VIS spectroscopy at 310 nm after the reaction with FeSO$_4$ solution (ESI†). The evolved H$_2$ gas was detected by using a thermal conductivity detector gas chromatograph (GC-8AIT, Shimadzu).

Results and discussion

Preparation and structural/optical properties of WO$_3$ nanosponge photoanodes

Fig. 1 shows the WO$_3$ nanoparticle morphology of the original and wet-ball milled samples (360 min). The original WO$_3$ nanoparticle diameter (*d*) was 20–200 nm (Fig. 1a), and included big nanoparticles with $d \approx 100$–200 nm and small nanoparticles with $d \approx 20$–50 nm. The original nanoparticles were wet-ball milled into smaller particles with a diameter of 5–150 nm (Fig. 1b), and the bimodal size distribution remained, with big nanoparticles with $d \approx 100$–150 nm and very small granular nanoparticles with $d \approx 5$–20 nm.

Fig. 2a shows photographs of the WO$_3$ nanoparticle dispersions. Dispersion D2, used to fabricate photoanode W2, was beige, and the dispersed nanoparticle size was evaluated by using a particle size analyzer to be mainly 264.1 nm in the range of 250–400 nm (Fig. 2b). This value indicates that the nanoparticles aggregated and were detected as secondary particles. We examined the effect of milling by preparing dispersions A, B, and C. Dispersion A was obtained by centrifuging and filtering (100 nm pore size) the original WO$_3$ nanoparticle dispersion in IPA (WO$_3$ nanoparticles were stirred vigorously in IPA). Dispersion B was obtained by centrifuging and filtering (100 nm pore size) dispersion D1, used to fabricate photoanode W1. Dispersion C was obtained by centrifuging and filtering (100 nm pore size) dispersion D2, used to fabricate photoanode W2. Dispersions A and B were completely transparent; however, a light suspension was visible in dispersion C. Under green laser irradiation, this colloidal suspension exhibited Tyndall scattering (Fig. 2a) that originated from very fine, highly monodisperse WO$_3$ nanoparticles with $d = 3.3$ nm, which corresponds to 4–5 unit cells of WO$_3$ (Fig. 2b). This means that wet-ball milling for 360 min produced very fine nanoparticles in the dispersion, whereas milling for 15 min did not. In the D3 dispersion (the WO$_3$ NPS hybrid dispersion) for the W3, the
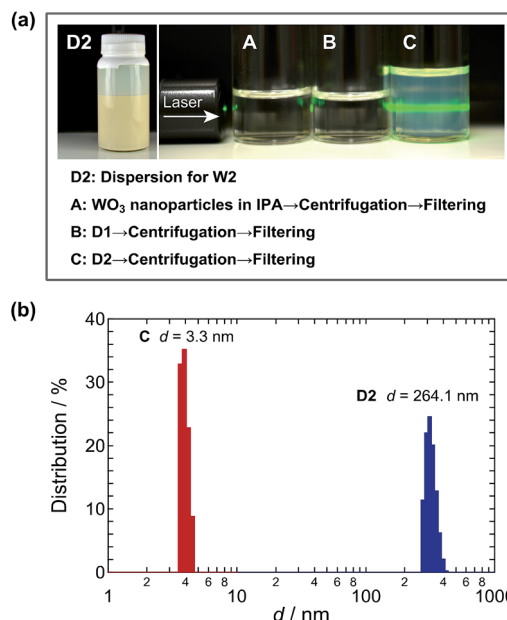

Fig. 2 (a) Photographs of the (O) WO$_3$ nanoparticle dispersion used for photoanode W2 and centrifuged/filtered dispersions A, B and C. The original sources of A, B and C were as follows: (A) original WO$_3$ nanoparticle dispersion in IPA (WO$_3$ nanoparticles were stirred vigorously in IPA), (B) dispersion W1 and (C) dispersion W2. The filtering of the centrifuged supernatant liquid was carried out by using 100 nm pore filters. (b) Particle diameter (*d*) distribution for the dispersion O and C.

solvated W ions from tungsten phenoxide were added to the WO$_3$ nanoparticle dispersion for D2 that contained very fine nanoparticles as seen in dispersion C.

The crystallinity and structure of photoanodes W1, W2, and W3, and the original WO$_3$ nanoparticles were analyzed by XRD (Fig. 3). The XRD pattern of the original WO$_3$ nanoparticles was from a pure γ-phase of WO$_3$ with a monoclinic $P2_1/c$ space group. The diffraction peaks were fitted without a specific crystal orientation by the Rietveld method by using RIETAN-FP,[36] and the unit cell parameters were refined as $a = 7.3204(5)$ Å, $b = 7.5301(5)$ Å, $c = 7.6917(5)$ Å, and $\beta = 90.67(1)°$, which were almost consistent with the reported values (JCPDS 20-1324 (ref. 37)). Photoanodes W1, W2, and W3 crystallised at 550 °C in the pure γ-phase of WO$_3$. Photoanode W3 showed preferential (001)-orientation growth, whereas photoanodes W1 and W2 exhibited almost no specific orientation.

Fig. 4 shows the FESEM for photoanodes W1, W2, and W3 at the WO$_3$ film surface and the interface between the WO$_3$ and FTO substrate. All the photoanodes had a granular morphology and 5–100 nm nanopores between the nanoparticles. Faceted-grown plate-like nanoparticles grew on the top surface of W3 (Fig. 4e), although the plate-like particles did not have a specific orientation in the films, as observed in the cross-sectional view (Fig. 4f). In contrast, no faceted-grown nanoparticles were observed in photoanodes W1 and W2, and they were more spherical (Fig. 4a–d). The preferential (001)-orientation growth observed in the XRD pattern of photoanode W3 originated from these faceted-grown (001)-face up plate-like nanoparticles on
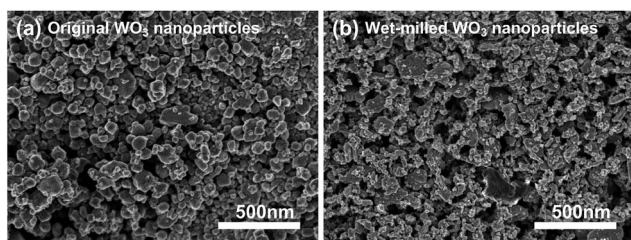

Fig. 1 FESEM images of nanoparticle morphology of WO$_3$ nanoparticles (a) before and (b) after wet-ball milling for 360 min.
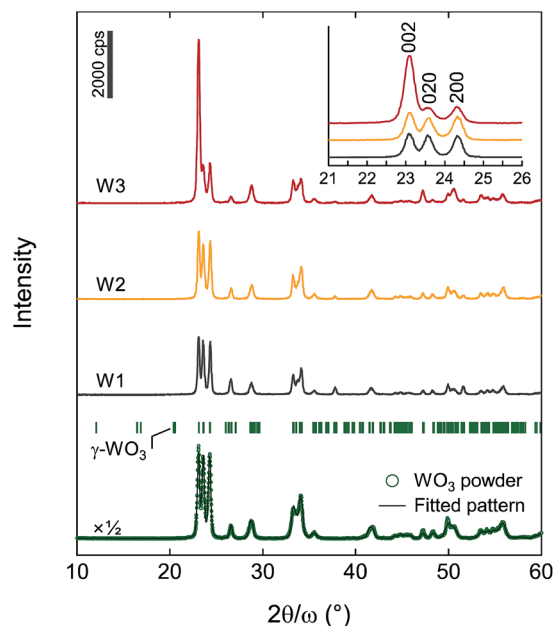
Fig. 3 XRD patterns of photoanodes W1, W2, and W3, and the original WO$_3$ nanoparticles. The diffraction pattern of the WO$_3$ nanoparticles was fitted by the Rietveld method. The vertical marks indicate the positions calculated for the Bragg reflections for γ-WO$_3$.
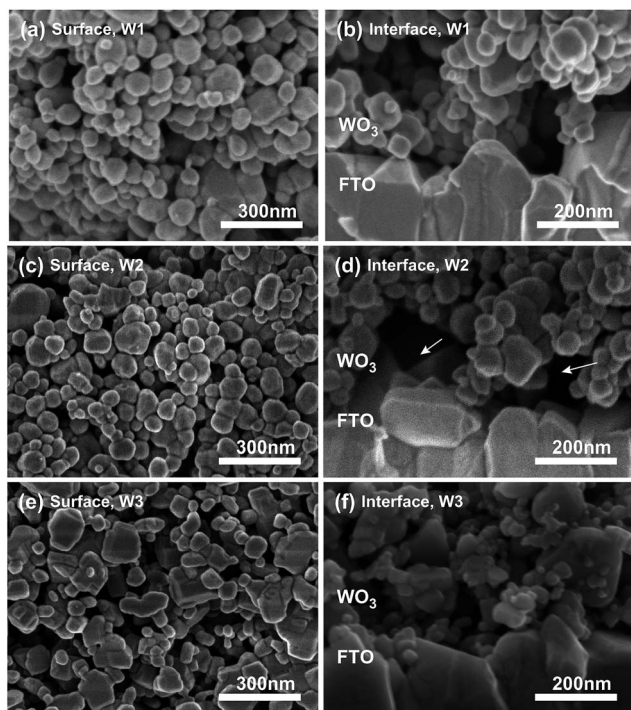

Fig. 4 FESEM images of the top surface of the WO$_3$ film and interface at the FTO glass substrate of the (a and b) W1, (c and d) W2 and (e and f) W3 films.

the surface. Therefore, there was an additional driving force for the crystal growth in photoanode W3. The W ions introduced by adding tungsten phenoxide to the WO$_3$ NPS hybrid dispersion ink spread effectively on the nanoparticles during firing, and

acted as an accelerator for crystal surface reconstruction, leading to the faceted growth. Another effect of tungsten phenoxide addition appeared at the interface between the WO$_3$ film and FTO glass substrate. In photoanode W3, very fine WO$_3$ nanoparticles covered the FTO glass surface, which was due to crystal nucleation from tungsten phenoxide solution. However, the interfaces had hollows with a size of approximately 100 nm in places in photoanodes W1 and W2. The high coverage of the top surface of the FTO bottom electrode facilitated effective excited electron transfer from the WO$_3$ layer.

The cross-sectional FESEM image of the whole of photoanode W3, including the FTO bottom electrode, is shown in Fig. 5a. The WO$_3$ film thickness was 7.4 μm with large numbers of nanopores (Fig. 4f and 5b), and the morphology was like a nanosponge. Microscopically the nanosponge consisted of large plate-like nanoparticles with an average size of 117 nm, and small granular nanoparticles with an average size of 23 nm (Fig. 5b). The large plate-like nanoparticles were bound by the small nanoparticles, and each particle had strong connections with distinct crystal grain boundaries. Thus, photoanode W3 exhibited the good crystallinity of WO$_3$ and finely connected nanoparticle networks with large numbers of nanopores. These features are desirable for excited electron/hole transfer.

Fig. 6 shows Tauc plots for photoanodes W1, W2, and W3, and original WO$_3$ nanoparticles that were evaluated from the transparency spectra obtained by using an integrating sphere. The band gap energy (E_g) of the source nanoparticles of 2.61 eV
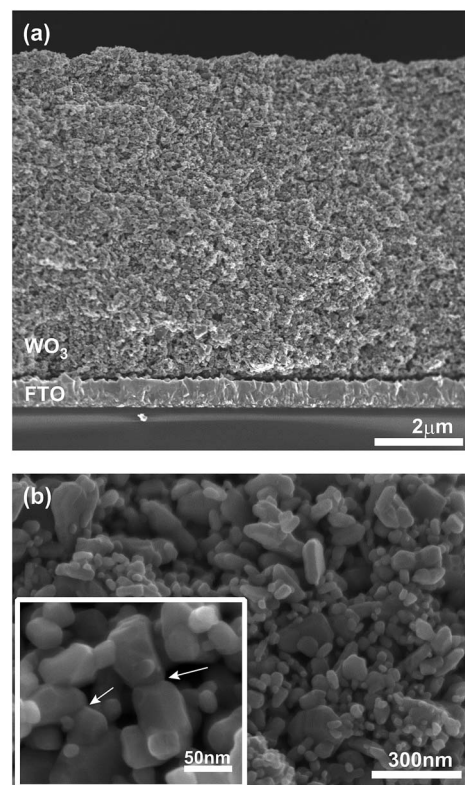

Fig. 5 Cross-sectional view of FESEM for photoanode W3. (a) Broad overview and (b) enlarged view of WO$_3$ nanoparticles. The white arrows indicate the grain boundaries of WO$_3$ nanoparticles.
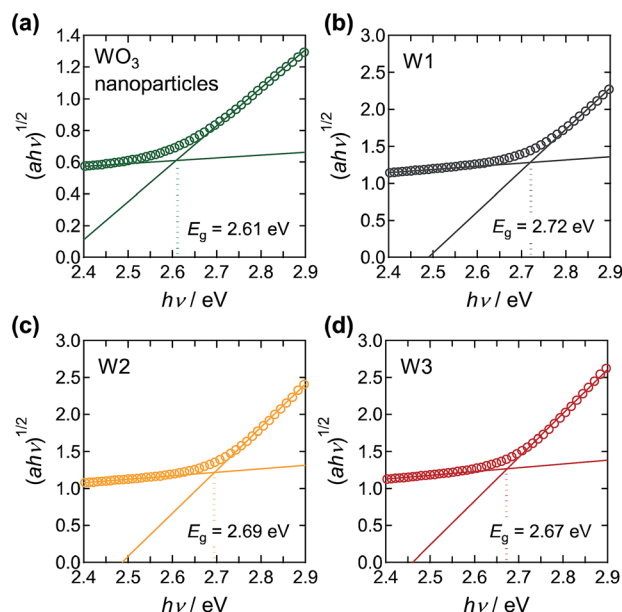
Fig. 6 Tauc plots for (a) WO$_3$ nanoparticles, (b) W1, (c) W2, and (d) W3.

was narrow compared with the literature value of WO$_3$ of 2.8 eV, indicating that there were defects in the crystal lattice of the nanoparticles. Photoanode W1 was fabricated from nanoparticle dispersion D1 that was subjected to short wet-ball milling (15 min), and firing at 550 °C recovered these defects to some extent. However, the finely crushed nanoparticles obtained by long wet-ball milling (360 min) that were used to fabricate photoanodes W2 and W3 retained slight surface defects owing to the large surface area of the very small diameter particles. Moreover, photoanode W3 contained small nanoparticles that originated from the pyrolysis and crystallisation of tungsten phenoxide. This increased the amount of very small nanoparticles, leading to a slight red shift in the absorption edge. The surface oxygen deficiency varied slightly between photoanode W1 and photoanodes W2 and W3. The reduced W^{5+} state was not detected by XPS by strong W^{6+} signals (Fig. S2†).[38] This means that there should be fewer oxygen defects than in photoanodes treated in reducing atmospheres.[39]

Fig. 7a shows the absorbance spectra of photoanodes W1, W2, and W3 collected with and without the integrating sphere. The optical band edges of each photoanode corresponded to the results of the Tauc plots (Fig. 6). However, a big difference was observed between the absorbance spectra of photoanode W1 and photoanodes W2 and W3 measured with and without the integrating sphere at wavelengths longer than 500 nm. In photoanode W1, a large pseudo-absorption was observed that arose from the incident light diffusion of the WO$_3$ layer above 500 nm. However, the absorption above 500 nm in photoanodes W2 and W3 was much smaller than that of photoanode W1 owing to the small light diffusion of the WO$_3$ layers. Photoanode W1 was light yellow compared with photoanodes W2 and W3 due to light diffusion (Fig. 7b). The incident white light (AM1.5G) was changed to red-orange by the relatively large transmission above 500 nm in photoanodes W2 and W3. The
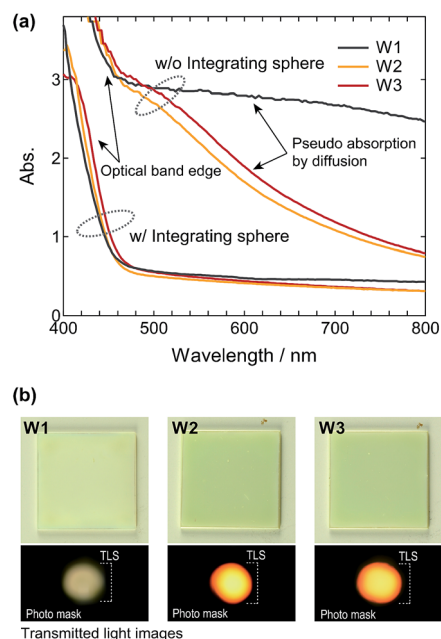

Fig. 7 (a) Absorption spectra of photoanodes W1, W2, and W3 collected with and without the integrating sphere. (b) Photographic images of W1, W2, and W3 photoanodes (top panel), and transmitted white light (AM1.5G) from the photoanodes through the photomask (bottom panel, TLS: transmitted simulated sunlight).

small light diffusion indicates that there were robust interconnections at the grain boundaries of the nanoparticles. Although the addition of tungsten phenoxide would affect the inter-nanoparticle bonding, the very small nanoparticles produced by the long wet-milling time of WO$_3$ nanoparticles (Fig. 2) would also play an important role by lowering the crystal growth temperature. The very small particles can reduce the melting temperature, as described by[40]

$$\Delta T = \frac{2\gamma_{ls}T_m}{\rho_s \Delta H_f r} \tag{2}$$

where ΔT is the melting point depression, γ_{ls} is the solid–liquid interface energy, T_m is the bulk melting point, ρ_s is the density of the solid, ΔH_f is the bulk heat of fusion, and r is the particle radius. Hence, ΔT of the small nanoparticles ($d \approx 3.3$ nm) was 30 to 45 times higher than that of large nanoparticles ($d \approx 100$–150 nm) according to this equation. It is unclear whether the small nanoparticles actually melted at 550 °C. However, the reactivity for liquid–solid or solid–solid sintering is increased by very small nanoparticles between the large nanoparticles in addition to the new nucleation and crystal growth by tungsten ions around the nanoparticles derived from the tungsten phenoxide solution (Fig. 8). Thus, we prepared WO$_3$ nanosponge layers with sufficient inter-nanoparticle bonding and many nanopores.

PEC properties of WO$_3$ nanosponge photoanodes for hydrogen and peroxydisulfate evolution under simulated sunlight

To evaluate the preparation conditions for optimising the PEC properties, we first examined the photocurrent density (j) of the
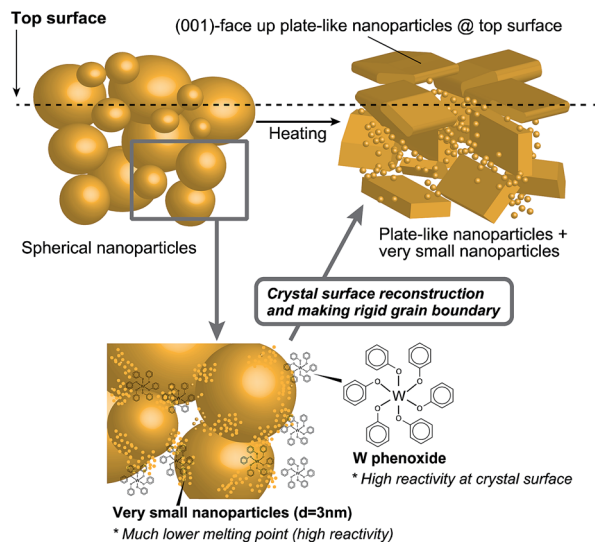
This journal is © The Royal Society of Chemistry 2016

J. Mater. Chem. A, 2016, **4**, 17809–17818 | **17813**

Fig. 8 Schematic illustration of crystal growth of W3 by NPS hybrid dispersion ink.

ca. 2 μm-thick WO₃ nanosponge photoanodes in aqueous 1 M H₂SO₄ solution under 1 Sun simulated sunlight from the front of the photoanodes at $1.5V_{RHE}$. Fig. 9 shows the dependence of J on the concentration of tungsten phenoxide in the WO₃ NPS

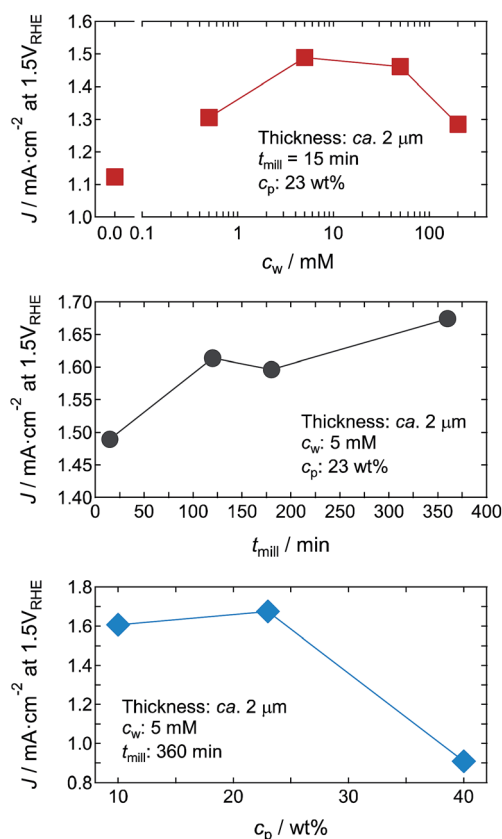hybrid dispersions (c_w), the wet-milling time (t_{mill}), and the concentration of WO₃ nanoparticles in the dispersions (c_p). c_w reached a maximum at 5 mM, and then J decreased with increasing concentration. This indicates that adding tungsten phenoxide improved the crystal quality of WO₃ nanosponges (Fig. 4f and 5). Excess tungsten phenoxide addition could reduce the surface area by filling the nanopores. We measured t_{mill} up to 360 min, and a long t_{mill} increased J because of the production of very fine nanoparticles that improved the inter-nanoparticle bonding. c_p affected the coating process. A high particle concentration was unsuitable for obtaining a homogeneous coating, and the optimum c_p was 10–25%. Thus, we concluded that the optimum conditions for a WO₃ nanosponge with high J were c_w = 5 mM, t_{mill} = 360 min, and c_p = 23 wt% (dispersion D3 in Table 1).

Fig. 10 shows the film thickness dependence of J under 1 Sun simulated sunlight from the front and back of the photoanodes at $1.5V_{RHE}$ for the WO₃ nanosponge photoanodes W1 and W3 prepared with dispersions D1 and D3, respectively (Table 1). For photoanode W1 prepared with dispersion D1, J measured under back illumination had a maximum (J_{max}) of 1.58 mA cm⁻² at 4.8 μm (Fig. 10a). Under front illumination, J was saturated up to 6–8 μm, and J_{max} was 1.22 mA cm⁻² at 5.8 μm. For WO₃ nanosponge photoanode W3 prepared by using dispersion D3,

Fig. 9 c_w, t_{mill}, and c_p dependences of J for WO₃ nanosponge photoanodes *ca.* 2 μm thick in aqueous 1 M H₂SO₄ solution under 1 Sun simulated sunlight from the front of the photoanodes at $1.5V_{RHE}$.
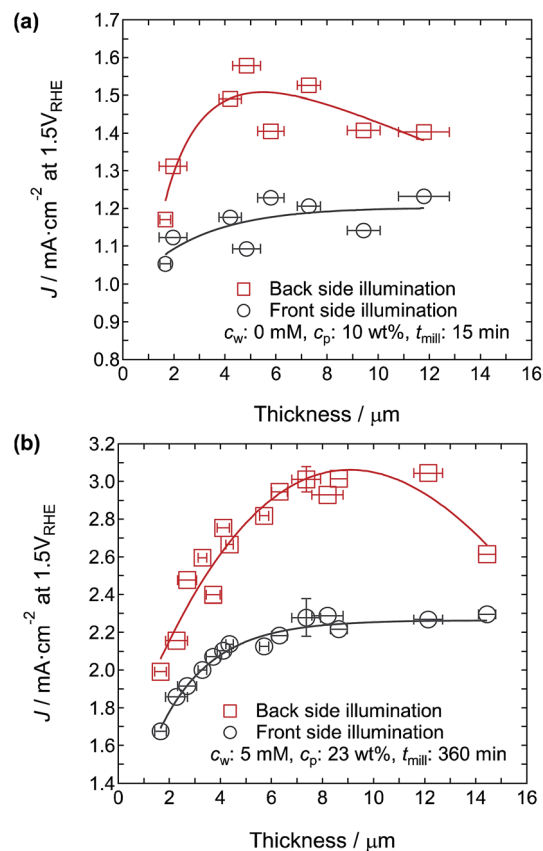
Fig. 10 Thickness dependence of J at $1.5V_{RHE}$ in 1 M H₂SO₄ electrolyte for the WO₃ films prepared from nanoparticle dispersions (a) D1 and (b) D3. The front and back of the WO₃ photoanodes were illuminated with incident light.

17814 | *J. Mater. Chem. A*, 2016, **4**, 17809–17818

This journal is © The Royal Society of Chemistry 2016

which was obtained by a long wet-milling time with tungsten phenoxide, J was markedly enhanced. Under front illumination, J was saturated up to 7 μm, and J_{max} was 2.28 mA cm^{-2} (average of 10 samples) at 7.4 μm (87% higher than J_{max} for photoanode W1). The J under the front illumination did not decrease below 15 μm; however, it will start decreasing at thicker thickness because of the limit of excitation penetration depth and long transporting distance of excited electrons. Under back illumination, J reached a maximum at 6–8 μm, and a J_{max} of 3.01 mA cm^{-2} was high (average of 10 samples) at 7.4 μm (91% higher than J_{max} for W1). Back illumination produces a high photocurrent because the photoexcited electrons can be transferred smoothly to the FTO bottom electrode.[41,42] The thickness dependence of J should be determined mainly by a competition between the light absorption and excited electron/hole transfer. The photoresponse of WO$_3$ nanosponges prepared by the D3 NPS hybrid dispersion showed a slight anodic shift with the increasing film thickness, and the thick WO$_3$ photoanode (14.4 μm) exhibited a gradual increase of the J–V curve (Fig. S3†). This indicated that too high photocarrier density near the bottom electrode due to the large film thickness could cause sluggish transport of excited electrons, resulting in the appearance of J_{max} in the thickness dependence of J. Nevertheless, J_{max} in the photoanode W3 prepared from dispersion D3 appeared thicker than photoanode W1 prepared from dispersion D1, suggesting that the WO$_3$ layer prepared from dispersion D3 effectively collected photoexcited electrons further from the bottom electrode. This arose from the good interparticle connections that allowed photocarrier transportation.

The J–V curves under chopped simulated sunlight at 1 Sun from the front of photoanodes W1, W2, and W3 were plotted (Fig. 11a). The onset potential of each photoanode was very similar at around 0.49V_{RHE}, and the J–V curves were saturated at around 1.1–1.2V_{RHE}. The J of W3 at 1.2V_{RHE} was 2.25 mA cm^{-2}, which was 60% and 13% higher than that of W1 and W2, respectively. Fig. 11b shows the J–V curves of the W3 under excitation from the front and back illumination. Although the onset potential under back illumination showed an anodic shift to 0.63V_{RHE}, J increased markedly to 3.04 mA cm^{-2} at 1.50V_{RHE}. This value is very high for a single junction photoanode, and reaches approximately half the theoretical limit of J under AM 1.5G illumination for the stoichiometric WO$_3$ with a band gap of 2.8 eV. The reported photocurrent densities of WO$_3$ photoanodes by using H$_2$SO$_4$ electrolyte are summarized in Table 2.

The photocurrent was maintained at $ca.$ 85% after 60 min, and it was recovered to the original photocurrent value by washing the photoanode (Fig. S4†). It could be mainly due to accumulation of the products in the inner photoanode nanostructure. The nanostructure of W3, $e.g.$, faceted nanocrystals and pore size, was unchanged before/after the reaction under 1 Sun illumination at 1.5V_{RHE} for 120 min (Fig. S5†); therefore, the obtained photoanodes would have sufficient stability for the use of this PEC reaction.

We performed Mott–Schottky and IMPS analyses of the effect of the physical properties of the photoanodes on the PEC performance. The Mott–Schottky plots for photoanodes W1, W2, and W3 exhibited n-type characteristics with a positive
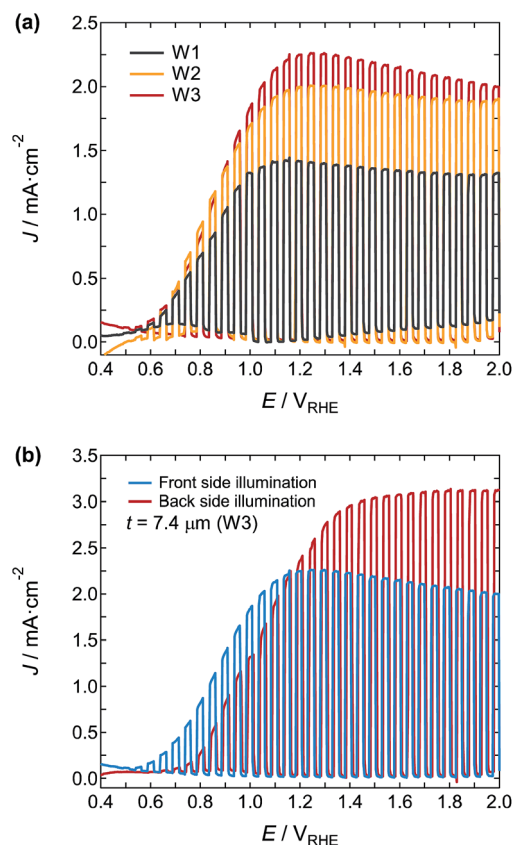
(a)

(b)

Fig. 11 (a) J–V curves under chopped simulated sunlight at 1 Sun in 1 M H$_2$SO$_4$ electrolyte from the front of the W1, W2, and W3 photoanodes. (b) LSV curves of the W3 photoanode illuminated with excitation light from the front and back.

slope (Fig. 12), indicating that electrons were the main carrier, as in n-type semiconductors. The curves were fitted by

$$1/C^2 = (2e_0\varepsilon_0\varepsilon N_d)(E - E_{FB} - kT/e_0) \tag{3}$$

where C is the space charge capacitance, e_0 is the electron charge, ε_0 is the vacuum permittivity, ε is the dielectric constant of WO$_3$ (= 20),[38] N_d is the donor density, k is the Boltzmann constant, T is the temperature, and E and E_{FB} are the applied and flat band potentials, respectively. The N_d of photoanodes W2 and W3 was 2.44 × 10^{21} and 3.06 × 10^{21} cm^{-3}, respectively (Table 3). These values were 30–40 times higher than that of photoanode W1. The high carrier density observed in photoanodes W2 and W3 could be due to the partial oxygen deficiency[51] at the WO$_3$ nanoparticle surface, as indirectly observed in the red shift of the optical absorption edges for photoanodes W2 and W3 (Fig. 6 and 7).

The electron transport in the photoanodes was evaluated by IMPS. Fig. 13a and b show the IMPS spectra of photoanodes W1, W2, and W3 under front and back illumination with UV LEDs at 365 nm. The photoexcited electron transport time (τ_e) is evaluated by an imaginary minimum (f_{min}) of the semicircles and is expressed as

$$\tau_e = 1/2\pi f_{min} \tag{4}$$

This journal is © The Royal Society of Chemistry 2016

J. Mater. Chem. A, 2016, 4, 17809–17818 | 17815

Table 2 Preparation conditions, nanostructure and PEC properties of WO$_3$ photoanodes in H$_2$SO$_4$ electrolyte

Preparation method	Nanostructure morphology[a]	Conc.[b]	Light source	J/mA cm^{-2}	Ref.
Chemical vapor deposition	Nanowire	0.5M	AM1.5G[c]	1.2 (1.2 V vs. SCE)	43
Hydrothermal	Spherical nanoparticles ($d = 60$ nm)	0.5M	AM1.5G[c]	0.6 (1.2 V vs. NHE)	44
Hydrothermal	Nanobar building blocks ($d = 60$ nm)	0.5M	AM1.5G[c]	1.87 (1.6 V vs. Ag/AgCl)	45
Pulsed laser deposition	Nanotree	1M	AM1.5G[c]	1.85 (0.8 V vs. RHE)	46
Plasma-assisted deposition	Nanofilament ($d = 100–200$ nm)	3M	AM1.5G[c]	1.0 (1.7 V vs. RHE)	47
Electrodeposition	Thin film ($t = 300$ nm)	1M	AM1.5G[c]	1.3 (1.4 V vs. NHE)	28
Chemical solution deposition	Spherical nanoparticles ($d = 50–100$ nm)	1M	AM1.5G[c]	2.6 (1.5 V vs. RHE)	29
NPS hybrid dispersion deposition	Plate-like nanoparticles ($d = 20–120$ nm)	1M	AM1.5G[c]	3.04 (1.5 V vs. RHE)	This work
Chemical solution deposition	Droplet-like particles ($d = 200–300$ nm)	1M	86 mW cm^{-2}	1.4 (1.2 V vs. SCE)	48
Chemical solution deposition	Nanoparticles ($d = 40$ nm)	1M	140 mW cm^{-2}	1.6 (1.4 V vs. SCE)	42
Anodization	Worm-like structure	1M	150 mW cm^{-2}	3.5 (1.5 V vs. SCE)	49
Anodization	Nanoporous ($d = 70–90$ nm)	0.5M	100 mW cm^{-2}	3.45 (1.6 V vs. Ag/AgCl)	50

[a] d and t represent the particle size and film thickness, respectively. [b] Concentration of H$_2$SO$_4$ electrolyte. [c] AM 1.5G: 100 mW cm^{-2}.
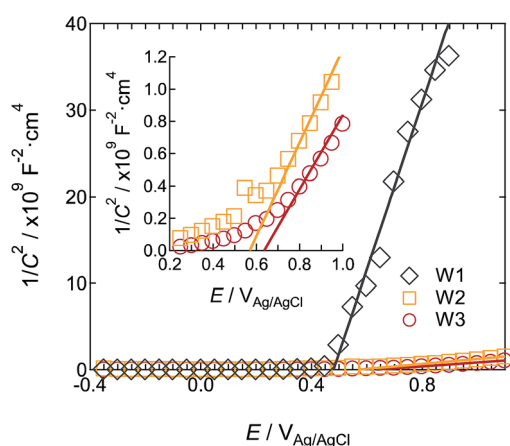

Fig. 12 Mott–Schottky plots of photoanodes W1, W2, and W3 at a frequency of 1.0 kHz in 1 M H$_2$SO$_4$ electrolyte.

Table 3 Calculated N_d, E_{FB}, and τ_e for photoanodes W1, W2, and W3

Sample	N_d/cm^{-3}	$E_{FB}/V_{Ag/AgCl}$	τ_e (front)/ms	τ_e (back)/ms
W1	7.32×10^{19}	0.48	7.11	0.63
W2	2.44×10^{21}	0.57	7.98	1.79
W3	3.06×10^{21}	0.67	8.95	5.65

The calculated τ_e values of photoanodes W1, W2, and W3 under front illumination were 7.11, 7.98, and 8.95 ms, respectively (Fig. 13c and Table 3). Back illumination made a large difference in τ_e of 0.63, 1.79, and 5.65 ms for photoanodes W1, W2, and W3, respectively (Fig. 13c and Table 3). Because of the short wavelength LED (365 nm) illumination, the penetration depth of excitation light was shallow, and the effect on transport time to the bottom electrode was maximised. The much longer transport time in photoanode W3 than in photoanodes W1 and W2 reflected the ease of charge transport from the regions further from the bottom electrode, suggesting that the good inter-nanoparticle connections played an important role in
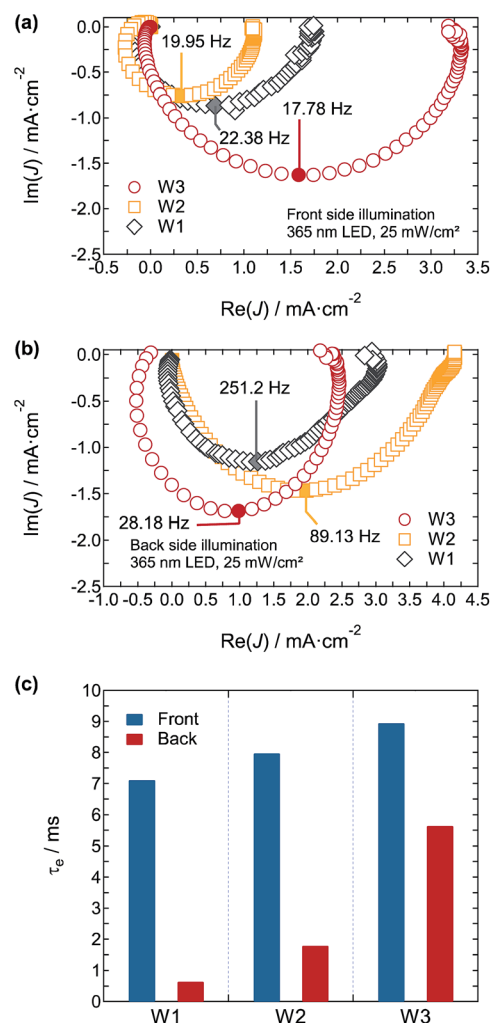

Fig. 13 IMPS responses of photoanodes W1, W2, and W3 biased at $1.5V_{RHE}$ in 1 M H$_2$SO$_4$ electrolyte under (a) front and (b) back illumination with the UV LED (365 nm). The LED was driven as a modulated light source with a DC intensity of 25 mW cm^{-2} and superimposed 10% AC intensity. (c) Photoexcited electron transport time τ_e for photoanodes W1, W2, and W3 under front and back illumination.

17816 | J. Mater. Chem. A, 2016, 4, 17809–17818

This journal is © The Royal Society of Chemistry 2016

increasing carrier transport. Based on the Mott–Schottky and IMPS analyses, photoanode W3 had a high carrier density and much better carrier transport, which affect the increase in photocurrent.

To evaluate the wavelength dependence of the PEC reaction in photoanode W3 in 1 M H_2SO_4 electrolyte, we measured the IPCE and APCE spectra (Fig. 14). As the wavelength of light decreased, the back illumination APCE spectra increased below 480 nm, and reached a high maximum of about 95.4% at 410 nm. This means that almost all the absorbed light was used for the PEC reaction around this wavelength. The APCE values were about 30% higher for back illumination than for front illumination, and it was almost independent of the wavelength. The IPCE values for back and front illumination were about 40% less than the APCE values. This arose from the light reflection of the WO_3 nanosponge photoanodes (Fig. S6†), and was linked to the decrease in J from the theoretical limit in photoanode W3. Therefore, the light harvesting properties in this system will be important for decreasing the gap between the current value and the theoretical limit.

We confirmed the generation efficiency of $S_2O_8^{2-}$ at the W3 photoanode and H_2 gas at the Pt cathode in 1 M H_2SO_4 electrolyte. The simulated sunlight was illuminated from the back of the photoanode. The Faraday efficiency of $\eta(S_2O_8^{2-})$ and $\eta(H_2)$ was calculated by $\eta(S_2O_8^{2-}/H_2) = $ (generated amount of $S_2O_8^{2-}(H_2)$/theoretical amount of $S_2O_8^{2-}(H_2)) \times 100$. Both $S_2O_8^{2-}$ and H_2 were stably generated under excitation light illumination, and stoichiometric evolution of $S_2O_8^{2-}$ and H_2 was confirmed as Faraday efficiencies of almost 100% (Fig. 15a and b). These results were consistent with previous reports.[28,29]

Finally, we measured the J–V curves with a two-electrode setup in 1.0 M H_2SO_4 electrolyte under 1 Sun illumination from the front and back of photoanode W3. Fig. 15c shows the calculated $ABPE_{S_2O_8^{2-}}$, and the maximum values for the back illumination of 2.45% at $1.26V_{CE}$ and 1.92% at $1.03V_{CE}$,
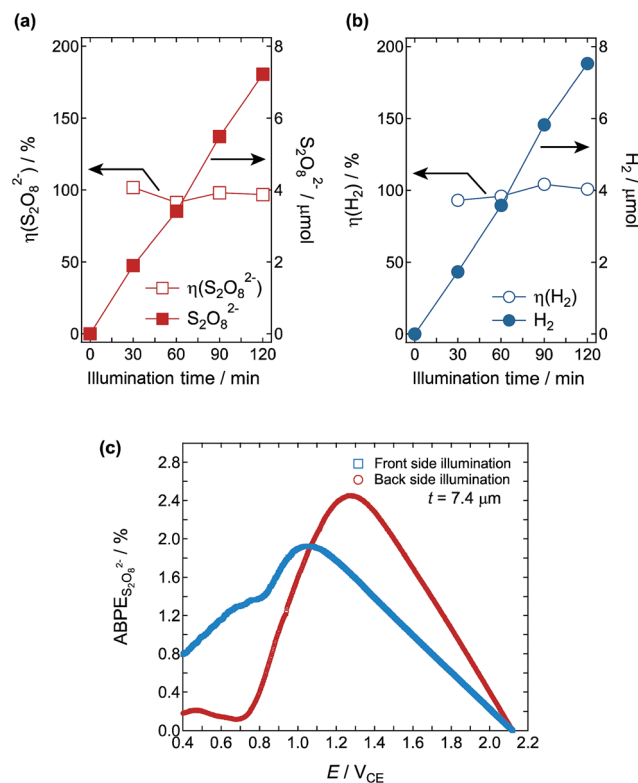

Fig. 15 Time dependence of Faraday efficiency and generated amounts of (a) $S_2O_8^{2-}$ (anode) and (b) H_2 (cathode). The reaction was carried out under 1 Sun simulated sunlight illumination from the back of the W3 photoanode with a steady photocurrent at 0.2 mA. (c) $ABPE_{S_2O_8^{2-}}$ calculated for the evolution of $S_2O_8^{2-}$ and H_2 in 1.0 M H_2SO_4 solution under simulated sunlight illumination from the front and back of photoanode W3.

respectively, were remarkably high. The 2.45% $ABPE_{S_2O_8^{2-}}$ is the highest efficiency reported for the production of $S_2O_8^{2-}$ and H_2.

Conclusions

We prepared WO_3 nanosponge photoanodes by NPS hybrid dispersion–deposition, and the WO_3 nanosponge photoanodes showed a large photocurrent (3.04 mA cm^{-2}) at $1.50V_{RHE}$ in 1.0 M H_2SO_4 electrolyte under 1 Sun back illumination of the photoanodes. This high photocurrent was obtained mainly because of the robust inter-nanoparticle connections and the preservation of the nanopores. The connections were produced by adding tungsten phenoxide and using very fine nanoparticles that were obtained by wet-milling. The APCE spectra showed a high maximum of about 95.4% at 410 nm. The PEC reaction of this system was confirmed as a stoichiometric reaction for $S_2O_8^{2-}$ and H_2 evolution, and $ABPE_{S_2O_8^{2-}}$ was calculated to be 2.45% at $1.26V_{CE}$ for the back illumination, which is the highest reported value. Obtaining this kind of high-value-added product at the photoanodes in PEC systems will be crucial for the sustainable industrial chemistry using sunlight.
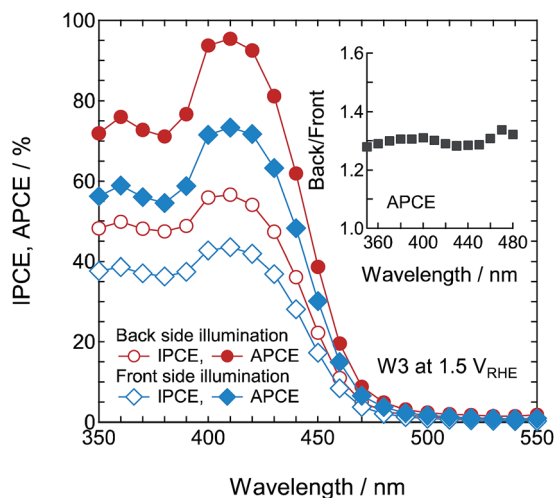

Fig. 14 IPCE and APCE spectra of photoanodes W1, W2, and W3 as a function of the excitation wavelength at $1.50V_{RHE}$ under front and back illumination. The inset shows the relative APCE under back illumination compared with front illumination.

This journal is © The Royal Society of Chemistry 2016

J. Mater. Chem. A, 2016, **4**, 17809–17818 | **17817**

Acknowledgements

Notes and references

1 Y. Tachibana, L. Vayssieres and J. R. Durrant, *Nat. Photonics*, 2012, **6**, 511.

2 A. Kudo and Y. Miseki, *Chem. Soc. Rev.*, 2009, **38**, 253.

3 T. Takata, A. Tanaka, M. Hara, J. N. Kondo and K. Domen, *Catal. Today*, 1998, **44**, 17.

4 A. Steinfeld, *Sol. Energy*, 2005, **78**, 603.

5 D. Gust, T. A. Moore and A. L. Moore, *Acc. Chem. Res.*, 2009, **42**, 1890.

6 T. Nakajima, T. Kitamura and T. Tsuchiya, *Appl. Catal., B*, 2011, **108–109**, 47.

7 B. D. Alexander, P. J. Kulesza, I. Rutkowska, R. Solarska and J. Augustynski, *J. Mater. Chem.*, 2008, **18**, 2298.

8 J. Nowotny, T. Bak, M. K. Nowotny and L. R. Sheppard, *Int. J. Hydrogen Energy*, 2007, **32**, 2609.

9 C. X. Kronawitter, L. Vayssieres, S. Shen, L. Guo, D. A. Wheeler, J. Z. Zhang, B. R. Antoun and S. S. Mao, *Energy Environ. Sci.*, 2011, **4**, 3889.

10 F. E. Osterloh, *Chem. Soc. Rev.*, 2013, **42**, 2294.

11 Y. Park, K. J. McDonald and K.-S. Choi, *Chem. Soc. Rev.*, 2013, **42**, 2321.

12 R. van de Krol, Y. Liang and J. Schoonman, *J. Mater. Chem.*, 2008, **18**, 2311.

13 T. Hisatomi, J. Kubota and K. Domen, *Chem. Soc. Rev.*, 2014, **43**, 7520.

14 T. Hisatomi, F. L. Formal, M. Cornuz, J. Brillet, N. Tétreault, K. Sivula and M. Grätzel, *Energy Environ. Sci.*, 2011, **4**, 2512.

15 X. Liu, F. Wang and Q. Wang, *Phys. Chem. Chem. Phys.*, 2012, **14**, 7894.

16 R. Saito, Y. Miseki and K. Sayama, *Chem. Commun.*, 2012, **48**, 3833.

17 B. A. Pinaud, P. C. K. Vesborg and T. F. Jaramillo, *J. Phys. Chem. C*, 2012, **116**, 15918.

18 T. Nakajima, T. Nakamura, K. Shinoda and T. Tsuchiya, *J. Mater. Chem. A*, 2014, **2**, 6762.

19 T. Nakajima, T. Nakamura and T. Tsuchiya, *Phys. Chem. Chem. Phys.*, 2014, **16**, 26901.

20 A. Fujishima, X. Zhang and D. A. Tryk, *Surf. Sci. Rep.*, 2008, **63**, 515.

21 M. Grätzel, *Nature*, 2001, **414**, 338.

22 M. R. Hoffmann, S. T. Martin, W. Choi and D. W. Bahnemann, *Chem. Rev.*, 1995, **95**, 69.

23 X. Chen, L. Liu, P. Y. Yu and S. S. Mao, *Science*, 2011, **331**, 746.

24 C. Yang, Z. Wang, T. Lin, H. Yin, X. Lü, D. Wan, T. Xu, C. Zheng, J. Lin, F. Huang, X. Xie and M. Jiang, *J. Am. Chem. Soc.*, 2013, **135**, 17831.

25 Z. Wang, C. Yang, T. Lin, H. Yin, P. Chen, D. Wan, F. Xu, F. Huang, J. Lin, X. Xie and M. Jiang, *Energy Environ. Sci.*, 2013, **6**, 3007.

26 R. Sathre, C. D. Scown, W. R. Morrow III, J. C. Stevens, I. D. Sharp, J. W. Ager III, K. Walczak, F. A. Houle and J. B. Greenblatt, *Energy Environ. Sci.*, 2014, **7**, 3264.

27 J. Nowotny, T. Bak, M. K. Nowotny and L. R. Sheppard, *Int. J. Hydrogen Energy*, 2007, **32**, 2609.

28 Q. Mi, A. Zhanaidarova, B. S. Brunschwig, H. B. Gray and N. S. Lewis, *Energy Environ. Sci.*, 2012, **5**, 5694.

29 K. Fuku, N. Wang, Y. Miseki, T. Funaki and K. Sayama, *ChemSusChem*, 2015, **8**, 1593.

30 K. Fuku and K. Sayama, *Chem. Commun.*, 2016, **52**, 5406.

31 T. Zhu, M. N. Chong and E. S. Chan, *ChemSusChem*, 2014, **7**, 2974.

32 C. A. Bignozzi, S. Caramori, V. Cristino, R. Argazzi, L. Meda and A. Tacca, *Chem. Soc. Rev.*, 2013, **42**, 2228.

33 A. Chen, T. F. Jaramillo, T. G. Deutsch, A. Kleiman-Scwarsctein, A. J. Forman, N. Gaillard, R. Garland, K. Takanabe, C. Heske, M. Sunkara, E. W. McFarland, K. Domen, E. L. Miller, J. A. Turner and H. N. Dinh, *J. Mater. Res.*, 2010, **25**, 33.

34 D. Zhang, T. Yoshida, K. Furuta and H. Minoura, *J. Photochem. Photobiol., A*, 2004, **164**, 159.

35 S. Kambe, S. Nakade, Y. Wada, T. Kitamura and S. Yanagida, *J. Mater. Chem.*, 2002, **12**, 723.

36 F. Izumi and K. Momma, *Solid State Phenom.*, 2007, **130**, 15.

37 B. O. Loopstra and H. M. Rietveld, *J. Solid State Chem.*, 1991, **91**, 286.

38 J. Yan, T. Wang, G. Wu, W. Dai, N. Guan, L. Li and J. Gong, *Adv. Mater.*, 2015, **27**, 1580.

39 T. Singh, R. Müller, J. Singh and S. Mathur, *Appl. Surf. Sci.*, 2015, **347**, 448.

40 R. M. German, *Liquid Phase Sintering*, Plenum Publishing Corporation, New York, 1985.

41 F. Amano, D. Li and B. Ohtani, *J. Electrochem. Soc.*, 2011, **158**, K42.

42 L. Meda, G. Tozzola, A. Tacca, G. L. Marra, S. Caramori, V. Cristino and C. A. Bignozzi, *Sol. Energy Mater. Sol. Cells*, 2010, **94**, 788.

43 V. Chakrapani, J. Thangala and M. K. Sunkara, *Int. J. Hydrogen Energy*, 2009, **34**, 9050.

44 S. J. Hong, H. Jun, P. H. Borse and J. S. Lee, *Int. J. Hydrogen Energy*, 2009, **34**, 3234.

45 S. K. Biswas and J.-O. Baeg, *Int. J. Hydrogen Energy*, 2013, **38**, 3177.

46 S. Shin, H. S. Han, J. S. Kim, I. J. Park, M. H. Lee, K. S. Hong and I. S. Cho, *J. Mater. Chem. A*, 2015, **3**, 12920.

47 M. de Respinis, G. D. Temmerman, I. Tanyeli, M. C. M. van de Sanden, R. P. Doerner, M. J. Baldwin and R. van de Krol, *ACS Appl. Mater. Interfaces*, 2013, **5**, 7621.

48 B. Yang, Y. Zhang, E. Drabarek, P. R. F. Barnes and V. Luca, *Chem. Mater.*, 2007, **19**, 5664.

49 V. Cristino, S. Caramori, R. Argazzi, L. Meda, G. L. Marra and C. A. Bignozzi, *Langmuir*, 2011, **27**, 7276.

50 W. Z. Li, J. Li, X. Wang, S. Luo, J. Xiao and Q. Y. Chen, *Electrochim. Acta*, 2010, **56**, 620.

51 S. K. Deb, *Phys. Rev. B: Solid State*, 1977, **16**, 1020.